Materials Advances

ROYAL SOCIETY OF CHEMISTRY

PAPER

View Article Online
View Journal | View Issue

Cite this: *Mater. Adv.*, 2022, 3, 4235

Enhanced up-conversion photoluminescence in fluoride–oxyfluoride nanophosphor films by embedding gold nanoparticles†

Thi Tuyen Ngo, Gabriel Lozano * and Hernán Míguez *

Received 21st January 2022,
Accepted 1st April 2022

DOI: 10.1039/d2ma00068g

rsc.li/materials-advances

Owing to their unique non-linear optical character, lanthanide-based up-converting materials are potentially interesting for a wide variety of fields ranging from biomedicine to light harvesting. However, their poor luminescent efficiency challenges the development of technological applications. In this context, localized surface plasmon resonances (LSPRs) have been demonstrated as a valuable strategy to improve light conversion. Herein, we utilize LSPR induced by gold nanoparticles (NPs) to enhance up-conversion photoluminescence (UCPL) in transparent, *i.e.* scattering-free, films made of nanophosphors formed by fluoride–oxyfluoride host matrix that feature high thermal stability. Transparency allows excitation by an external source without extinction losses caused by unwanted diffuse reflection. We provide a simple method to embed gold NPs in films made of YF/YOF:Yb^{3+},Er^{3+} UC nanophosphors, *via* preparation of a viscous paste composed of both UC nanophosphors and colloidal gold NPs, reducing complexity in sample fabrication. The dimensions of gold NPs are such that their associated LSPR matches spectrally with the green emission band of the Er^{3+} doped nanophosphors. In order to demonstrate the benefits of plasmonic nanoparticles for UCPL in nanophosphor films, we provide a careful analysis of the structural properties of the composite thin films along with precise characterization of the impact of the gold NPs on the photophysical properties of UC nanophosphors.

Introduction

Rare earth-activated up-converting materials, typically composed of an inorganic host matrix doped with lanthanide ions, *e.g.*, Er^{3+}, Ho^{3+}, and Tm^{3+}, have attracted a great deal of scientific and industrial interest due to their unique non-linear optical character.[1] Their long emission lifetime, narrow emission bandwidth and excellent photo-stability, result from the 4f transitions of lanthanide ions, which allow them to have enormous potential for different fields including biomedicine,[2] light harvesting,[3] super-resolution microscopy[4] and color display.[5] However, these materials present relatively low brightness due to the intrinsically inefficient non-linear process,[6] and their small absorption cross-section,[7,8] which is challenging when developing practical applications based on up-conversion (UC) nanotechnology.

Several strategies to overcome the above-mentioned issues have been designed in recent years. Most of them are related to the optimization of the material composition and chemical structure, including surface passivation through core–shell architectures,[9] dopant optimization[10] or host engineering.[11] Other strategies involve modification of the optical environment of the UC materials. Among these, localized surface plasmon resonances (LSPRs)[12] induced by metallic nanoparticles (NPs) appear as a valuable alternative to modulate the emission of up-converting materials.[13–16] When metallic NPs are illuminated, the electron cloud oscillates within the skin depth of the metallic NP, which produces a significant enhancement of the electric field intensity in the proximity of the resonant NP. For up-converting nanoparticles (UCNPs) located in the proximity of the metallic NP, such electric field enhancement can modify the fraction of the incident light that nanomaterials absorb if LSPR matches the excitation band of the UC material, but also alter the dynamics of electron transitions between the ground and excited states if metallic NPs are chosen to be resonant with the emission of the UC materials.[14]

Several experimental demonstrations of the use of LSPRs to enhance UCPL have been reported recently.[17–21] In fact, it has been shown that aqueous solutions of different core/shell heterostructures in which thin layers of gold or Au/SiO_2 nanorods, capable of supporting LSPRs that match the emission or excitation band of UCNP, allow enhancing UCPL.[17,18] Metallic

Instituto de Ciencia de Materiales de Sevilla, Consejo Superior de Investigaciones Científicas (CSIC) – Universidad de Sevilla (US), Américo Vespucio, 49, 41092 Sevilla, Spain. E-mail: g.lozano@csic.es, h.miguez@csic.es

† Electronic supplementary information (ESI) available. See DOI: https://doi.org/10.1039/d2ma00068g

NPs have been also successfully combined with UC materials deposited as films or integrated into more complex architectures. For instance, inorganic nanowires coated with Au nanorods have proven useful to improve the emission of UCNPs deposited atop.[19] Also, the surface of a three-dimensional photonic crystal was coated with UCNPs and gold nanorods to prove a significant increase in the UCPL due to a combined plasmonic/photonic effect.[20] In another example, SiO_2 microbeads decorated with Ag NPs coated with UCNPs have demonstrated enhanced absorption and UCPL.[21] However, most of the proposed approaches involve complex preparation techniques, which compromise their applicability.

Herein, we combine gold NPs and fluoride–oxyfluoride UCNPs in a single film following inexpensive solution-based preparation routes, and study UCPL. We use a fluoride–oxyfluoride matrix as the host material because these matrices exhibit high conversion efficiencies typical of fluorides along with the thermal stability associated with oxides.[22] Notice that thermal stability becomes particularly relevant for applications where high-power lasers are used as the excitation source. Central to our approach is the development of unprecedented optically transparent (*i.e.*, scattering free) films made of UCNPs, capable of hosting plasmonic particles and allowing their excitation by an external source without extinction losses caused by unwanted diffuse reflection. Hence, the LSPR of gold NPs is targeted to be resonant with the emission band of the UCNPs. Enhancement of the up-conversion effect is observed and its plasmonic origin confirmed by the combined analysis of the spectral dependence of the gold NP modified UCPL and its decay dynamics. Furthermore, the effect of LSPRs on the interplay between excitation and relaxation processes occurring in the UCNPs is discussed on the basis of the changes observed in the power dependence relation between excitation power and emitted UCPL intensity.

Results and discussion

Gold nanoparticle-loaded nanophosphor films

Yttrium fluoride NPs co-doped with ytterbium and erbium (YF_3:Yb^{3+},Er^{3+}) NPs were synthesized following a procedure reported elsewhere.[22] Their transmission electron microscopy (TEM) image is displayed in Fig. S1a (ESI†), showing that YF_3:Yb^{3+},Er^{3+} NPs are uniform and present an ellipsoid-like morphology, with a mean long dimension of 152 nm ± 15 nm. In order to prepare nanophosphor films based on those NPs, we develop nanocrystal-based pastes by mixing the phosphor NPs with an organic binder, see the schematic processing in the left side of Fig. 1a.[23,24] To embed metallic NPs in nanophosphor films, gold colloids (see Fig. S2 of the ESI†) were introduced into the YF_3:Yb^{3+},Er^{3+} suspension during the paste preparation, see the schematic processing in the right side of Fig. 1a. Full details are provided in the Experimental section. Nanophosphor films without and with embedded gold NPs were fabricated by blade coating (see Fig. 1b). This method allows obtaining mechanically stable and uniform films of controlled thickness. The top view Scanning Electron Microscopy (SEM) image of a representative nanophosphor film devoid of gold nanoparticles is displayed in Fig. S1b (ESI†). The image reveals a flat surface and a connected nanocrystal network. Also, film processing does not alter the shape and size of the nanophosphors. Fig. 1c and d present the top view SEM

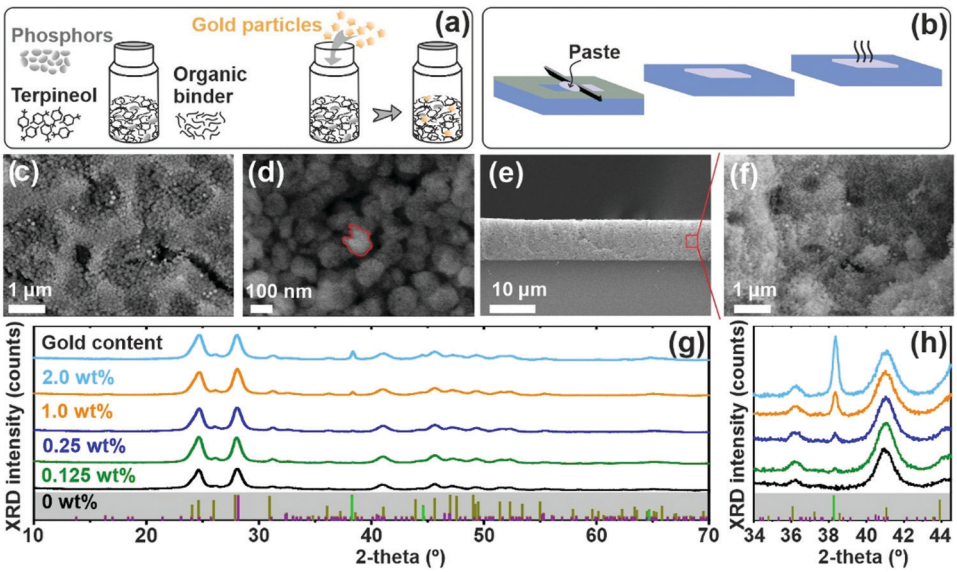

Fig. 1 (a) Schematic of the paste preparation method. (b) Sketch of the film processing. (c–f) SEM images with different magnifications of a top view (c and d) and a cross section (e and f) of a nanophosphor film that contains 2 wt% of gold NPs. A single gold NP is highlighted with a red line in (d). (g) XRD pattern of nanophosphor films with different contents of gold NPs. Reference patterns included in (g and h) are YF_3 (dark yellow vertical lines, power diffraction reference (PDF) No. 00-032-1431), $Y_7O_6F_9$ (purple vertical lines, PDF No. 01-070-0867) and Au (green vertical lines, reference No. 00-001-1172). (h) Details of (g) to highlight the Au signal.

images of a nanophosphor film with 2.0 wt% of embedded gold NPs with different magnifications. In particular, gold NPs appear as bright dots in Fig. 1c. Elemental analysis of the region shown in Fig. 1d further confirms the presence of gold in the film (see Fig. S1c of the ESI†). Fig. 1e and f and Fig. S1d–h (ESI†) show the SEM images of a cross section and pictures of nanophosphor films with different amounts of embedded gold NPs, which can be identified as bright dots in Fig. 1f. All films are uniform with a thickness around 5 μm. Nevertheless, we observe that the presence of gold NPs induces a certain increase in the porosity of the films along with their thickness (see Fig. S1d–g (ESI†)). We determined the crystalline structure of our nanophosphor films by performing X-ray diffraction (XRD) measurements. Full details are provided in the Experiment section. Fig. 1g and h display XRD patterns of films with different contents of embedded gold NPs. Analysis reveals that the films present a two-phase mixture of orthorhombic YF_3 (Powder Diffraction File (PDF) No. 00-032-1431)[25] and orthorhombic $Y_7O_6F_9$ (PDF No. 01-070-0867).[22] The formation of orthorhombic $Y_7O_6F_9$ is due to the inherent instability of the fluoride host. During annealing in an air atmosphere, O atoms replace F ones and are incorporated in the lattice.[26,27] Notice that the intensity of the diffraction peaks and their full width at half-maximum (FWHM) are very similar for all samples, which indicates that all nanophosphor films feature similar crystallinity regardless of their gold content. In addition, the higher peak intensity of the gold signal (reference No. 00-001-1172) is observed for nanophosphor films with a larger embedded gold content, as highlighted in Fig. 1h.

Spectroscopic analysis of the up-conversion photoluminescence

Fig. 2a and b present the total transmittance and absorptance measurements of nanophosphor films with different contents of embedded gold NPs. A broad band, between ~450 nm and ~800 nm, associated to the LSPR of gold NPs is clearly observed for gold-containing films.[18,19,28–30] Notice that the intensity of the band increases with the gold content in the nanophosphor films. Moreover, its spectral position slightly shifts to the red (from 523 to 540 nm) for the films with the highest loading, which can be associated with dipole coupling of plasmon modes in individual NPs.[31] However, for low amounts of gold, *e.g.* 0.125 and 0.25 wt%, the extinction peak increases but its spectral position barely changes, as shown in Fig. 2. We attribute this deviation to a certain lack of uniformity in the films for a low gold concentration. Similar features are observed in the reflectance spectra (see Fig. S3a (ESI†)). Additionally, the insets in Fig. 2a and b show a dip in transmittance associated to an absorption peak at ~980 nm which is correlated to $^2F_{7/2}$–$^2F_{5/2}$ transition of the Yb^{3+} ions.[2,32,33] Please note that (i) the reference film's average transparency (around 90%, see Fig. S1h, ESI†) is preserved to a great extent after the

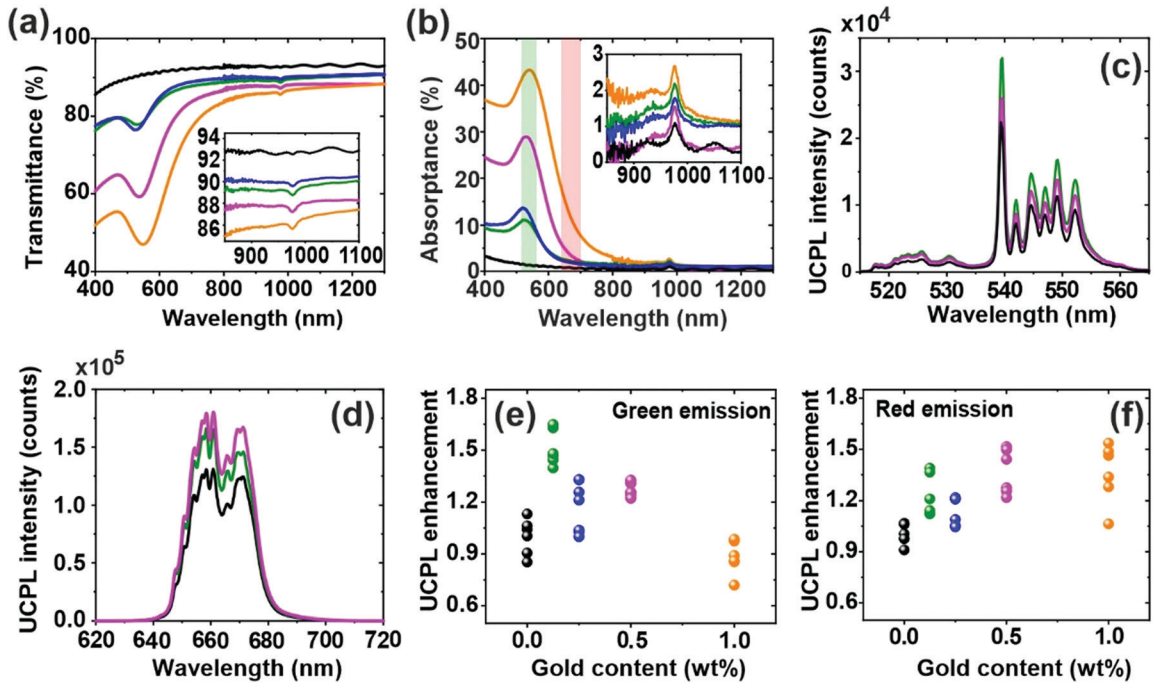

Fig. 2 (a) Experimental total transmittance, (b) absorptance, and (c and d) average UCPL intensity spectra of nanophosphor films containing gold NPs with different loadings. This is 0.125 wt% (green curve), 0.25 wt% (blue curve), 0.5 wt% (purple curve) and 1.0 wt% (orange curve). Measurements on a reference layer (devoid of gold NPs) is also displayed for comparison as a black curve. Green and red UCPL emission bands are highlighted as shaded areas in (b). (e and f) Integrated UCPL intensity enhancement as a function of gold content for each emission band. UCPL intensity is integrated between 510 and 570 nm for the green band, and between 620 and 720 nm for the red emission band. To calculate the enhancement at each loading, integrated values are divided by the average integrated UCPL intensity of the reference nanophosphor films. UCPL measurements are performed using a 980 nm (~45.0 W cm^{-2}) continuous wave laser as the excitation source.

inclusion of gold NPs in the spectral region where no LSPR associated extinction is expected ($\lambda > 800$ nm) and (ii) the absorption at $\lambda \sim 980$ nm of the nanophosphor films, which can be estimated from the depth of the transmission dip, is nearly identical regardless the gold loading (see Fig. S3b, ESI† for a more detailed analysis of this feature), which indicates the absence of plasmonic enhancement effects in this region.

In order to analyze the emission properties of nanophosphor films with and without the embedded gold NPs, we use a 980 nm laser as an excitation source that matches the $^2F_{7/2}$–$^2F_{5/2}$ transition of the Yb^{3+} ions. Fig. 2c and d display their green and red emission bands, which are associated with the transitions of $^4S_{3/2}$, $^2H_{11/2}$; and $^4F_{9/2}$ to the ground state $^4I_{15/2}$ of Er^{3+} ions, respectively (see Fig. S4 of the ESI†). Our films also present a weak blue emission band, see Fig. S3c (ESI†), corresponding to the $^2H_{9/2}$–$^4I_{15/2}$ transition of Er^{3+} ions.[2,10,34,35] The detection of these visible emission bands of Er^{3+} transitions by excitation through Yb^{3+} ions confirms the UC mechanism, with energy transferred between the $^2F_{5/2}$ and $^4I_{11/2}$ levels of Yb^{3+} and Er^{3+} ions.[10,36–40] Our results also show that embedding gold NPs in nanophosphor films leads to a spectrally sensitive UCPL enhancement, which is dependent on the gold content and different for each emission band, as shown in Fig. 2e and f. A statistical analysis of the integrated UCPL intensities was performed by normalizing them to the average of the UCPL intensity of the reference nanophosphor films (devoid of gold colloids). Notice that the spectral position of the LSPR overlaps well with the green emission band of the nanophosphors (green shaded region in Fig. 2b), which enables energy transfer between the nanophosphors and the plasmonic particles.[41,42] However, this transfer depends strongly on the average distance between luminescent centers and metallic NPs,[18,29,43,44] which is affected by the concentration of gold NPs in the film. The intensity of UCPL depends on two distinct processes: (i) the feeding of Er^{3+} levels, and (ii) the relaxation to the ground state, which can be radiative and nonradiative. Gold NPs might accelerate the population of the Er^{3+} intermediate level and enhance the radiative rate, but at the same time gold excess can also lead to UCPL quenching. As a result, for the green emission band, the UCPL enhancement reaches the highest value ($\sim$1.7 fold) for low gold loading (see Fig. 2e), which is associated to an increase in the radiative decay rate of Er^{3+}.[14,41,45] The enhancement gradually reduces with gold content. As a matter of fact, the presence of gold NPs brings about absorption losses and introduces non-radiative decay channels that are detrimental for the UCPL, as previously reported for $NaYF_4$:Yb,Er NPs decorated with Ag NPs.[46] In contrast, for the red emission band (red shaded region in Fig. 2b), UCPL is enhanced roughly by $\sim$30% for gold-containing films, as shown in Fig. 2f. Since the Er^{3+} red emission band only overlaps with the tail of the LSPR, the contribution of plasmon emission enhancement is expected to be low. In this case, the improvement of the UCPL can be mainly attributed to a combination of near field effects and improved outcoupling due to plasmonic scattering.

Up-conversion photoluminescence dynamics

In order to shed some light on the mechanism behind the UCPL enhancement observed, time-dependent measurements are performed. We monitor the green emission band of nanophosphors, associated to transitions of $^4S_{3/2}$ and $^2H_{11/2}$ to the ground state $^4I_{15/2}$ of Er^{3+} ions, which matches well with the LSPR of gold NPs. A two-exponential model

$$I(t) = A_1 e^{-t/\tau_1} + A_2 e^{-t/\tau_2}$$

is employed to describe the PL dynamics of nanophosphors. It accounts for the two different decay rates (τ_1^{-1} and τ_2^{-1}) expected for Er^{3+} cations located in each crystalline lattice (YOF and YF). A_1 and A_2 are fitting constants associated with the relative weight of each contribution to the sum. The average lifetime is calculated using the following equation

$$\tau = \sum A_i \tau_i^2 \Big/ \sum A_i \tau_i$$

This model has been recently proven as a useful tool to correlate the structural and optical properties of UC nanophosphor films.[22] The results are shown in Fig. 3 and Table S1 (ESI†). The average lifetime of green Er^{3+} transitions, $^4S_{3/2}$ and $^2H_{11/2}$ to the ground state $^4I_{15/2}$, devoid gold NPs is $\sim$46 μs, as it

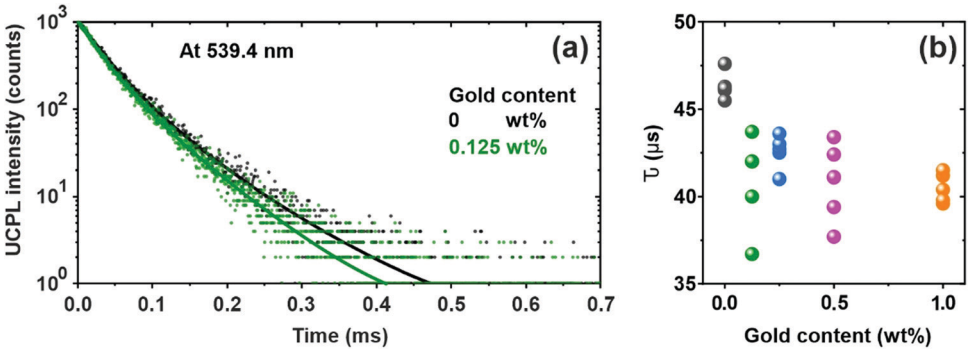

Fig. 3 (a) Time dependence of the UCPL of nanophosphor films with embedded gold NPs (green dots) and devoid them (black dots). Their corresponding fitting curves are also shown as solid lines. (b) Extracted average lifetime as a function of gold content. A 980 nm pulsed laser is used as an excitation source. Emission is collected at 539.4 nm.

has been reported for similar host crystal phases.[27,47] The introduction of plasmonic colloids leads to the reduction of the lifetime components (τ_1 and τ_2) and, thus, the average lifetime of Er^{3+}, which originates from the fast decay channels introduced by the metal. Average lifetime reduction is more pronounced for the film in which gold NPs are embedded with 0.125 wt%. Interestingly, the reduction of the lifetime for each component is very similar (~10%), see Fig. S5 (ESI†), indicating plasmonic colloids influence green Er^{3+} transition regardless of the crystal lattice site where Er^{3+} ions sit. This enhanced radiative decay rate, γ, along with an increase in the UCPL intensity shown in Fig. 2e, unambiguously indicates an increase of the local photon density of states, ρ_{LDOS}, which is expected to occur in the vicinity of plasmonic particles.[13,48–50] This phenomenon, also known as Purcell effect, is a direct consequence of Fermi's Golden rule, formally expressed by the formula:[51]

$$\gamma = \frac{2\omega}{3\hbar\varepsilon_0}|\mu|^2\rho_{LDOS}(r,\omega)$$

in which the spectral and spectral dependence of the ρ_{LDOS} is explicitly indicated, $\hbar$ is the reduced Planck constant, ε_0 is the vacuum permittivity and μ is the transition dipole moment corresponding to the electronic transition of frequency ω.

Power-dependent photoluminescence

UC materials feature a unique dependence of the emission intensity with the excitation power, which originates from the interplay between relaxation and energy transfer processes involved in the UC mechanism.[52–54] In order to investigate the influence of the metallic NPs on the nonlinear nature of the UC process, we measure the UCPL of the green and red emission bands for different values of the excitation power. Details are provided in the Experimental section. Fig. 4a shows the integrated green and red UCPL intensity of a reference (devoid gold NPs) UC nanophosphor film as a function of the excitation power. UCPL associated with the green and red emission bands increases quickly with power.[55,56] A similar behavior is observed for phosphor films with embedded gold NPs, see Fig. S6 and S7 (ESI†). UCPL power-dependence originates from the depopulation of the $^4I_{11/2}$ intermediate energy level of Er^{3+} due to competition between (i) the energy transfer up-conversion (ETU) rate to high-energy levels of Er^{3+} ions, and (ii) relaxation to the ground state, see Fig. S4 (ESI†).[57] In the weak power regime, relaxation dominates over ETU and UCPL exhibits a quadratic power dependence associated with the sequential absorption of two photons. Indeed, data shown in Fig. 4a can be fitted with a slope of ~2.0. Above a certain energy threshold, the $^4I_{11/2}$ intermediate level saturates, because of the fast energy transfer rate from the Yb^{3+} sensitizer and, thus, UCPL is achieved by the absorption of only one photon, following a linear power dependence.[53,55] The power density at which the transition between the quadratic and linear regime occurs is known as the critical power density (CPD), and it has been demonstrated to be affected by plasmonic resonances.[49] The power dependence of UCPL intensity has been widely studied and most reports show a quadratic (linear) dependence in the low (high) excitation power range. However, specific values of the excitation power density used are very different in each study ranging from ~1 W cm^{-2},[52] 1–10 kW cm^{-2},[57,58] to ~100 kW cm^{-2}.[49,59] Such differences may originate both from the intrinsic efficiency of the different UC materials under study and the collection efficiency of the experimental setups used to record the signal in each case. Although our excitation source is not powerful enough to reach CPD, we find that fitted slopes for both red and green emission bands reduce with the gold content, as plotted in Fig. 4b and c. Slope reduction induced by LSPR has been already observed for YF_4:Yb–Er UC particles deposited on gold nanorods[20] and for YF_4:Yb–Er based nanocavities.[59] However, its physical origin remains elusive. Herein we speculate that slope reduction with gold content may be related to the transition between quadratic and linear excitation regimes. Indeed, we consider that LSPRs might accelerate the energy transfer from the $^2F_{5/2}$ energy level of Yb^{3+} to the $^4I_{11/2}$ of Er^{3+}, see Fig. S4 (ESI†). Consequently, saturation of this intermediate energy level is easier to reach, as the transition between quadratic and linear excitation regimes is gradually accelerated. This is in agreement with the study of

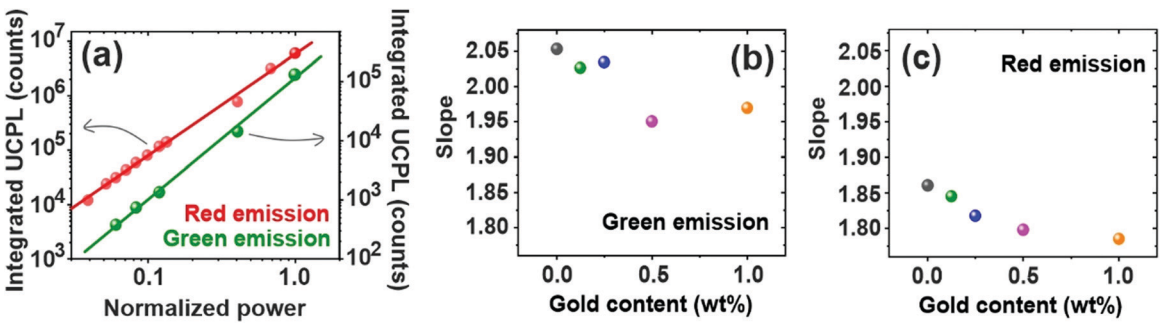

Fig. 4 (a) Integrated UCPL intensity as a function of the excitation laser power (colored dots) for the red UC band (between 620 nm and 720 nm) and the green one (between 510 and 570 nm) of UC nanophosphor film without gold NPs. Fittings are shown as solid lines. The films are excited with a 980 nm continuous wave laser operating at full power. A computer-controlled neutral density filter wheel is used to attenuate the output of the laser and excite the films at a lower excitation power. (b and c) Extracted value of the slope obtained from the fitting of the power dependence UCPL as a function of gold content for green (b) and red emission bands (c).

Andersson-Engels and co-workers[57] in which they point out that there is a gradual shift between power regimes, existing in an intermediate excitation power range in which the slope goes from 2.0 to 1.0 in a continuous manner. Finally, we observe that the slope of the red emission band is smaller than that of the green for all nanophosphor films. It has been reported that the CPD of red emission is lower than that of the green band,[52] which has been attributed to the feeding mechanism of the $^4F_{9/2}$ energy level. Concretely, the $^4I_{11/2}$ intermediate level relaxes to $^4I_{13/2}$ and then ETU occurs from this level to $^4F_{9/2}$, see Fig. S4 (ESI†). Besides, there is a minor contribution of the relaxation from $^2H_{11/2}$ and $^4S_{3/2}$ energy levels to the $^4F_{9/2}$, which increases for a high excitation power,[32,52] which is responsible for the different CPD observed for the red and green emission bands.[52]

Conclusions

We have developed a simple method to prepare uniform up conversion (UC) films with embedded gold NPs, which are resonant with the emission bands of Er^{3+}. We investigate the effect of LSPR induced by gold NPs on the photophysical properties of UC films. The introduction of gold NPs does not alter the crystalline structure of the UC material but strongly influences the UC photoluminescence of the nanophosphors. We observe that the green emission band of Er^{3+} is improved at a low gold content due to an enhanced radiative decay rate. Increasing gold content causes, in turn, a reduction in the green UCPL enhancement due to the absorption of gold NPs. In contrast, the red emission band of Er^{3+}, spectrally detuned from the LSPR, is hardly affected by the plasmonic colloids, which highlights the physical origin of the UC emission enhancement observed. Besides, the analysis of the influence of embedded gold NPs on the power-dependence of the UCPL intensity reveals that increasing gold content reduces the quadratic dependence typically expected for these systems. We argue that such reduction is due to a faster saturation of the $^4I_{11/2}$ intermediate energy level of Er^{3+} caused by a plasmonic-mediated enhanced energy transfer from the $^2F_{5/2}$ level of Yb^{3+}. Our study shed light on the influence of plasmonic resonances in UC.

Experimental section

Chemicals

For the synthesis of up-converting nanoparticles, yttrium(III) chloride hexahydrate ($YCl_3{\cdot}6H_2O$, Sigma-Aldrich, 99.9%), erbium(III) chloride hexahydrate ($ErCl_3{\cdot}6H_2O$, Sigma-Aldrich, 99.9%) and ytterbium(III) chloride hexahydrate ($YbCl_3{\cdot}6H_2O$, Aldrich, 99.9%) were selected as lanthanide (Ln) precursors. 1-Butyl, 3-methylimidazolium tetrafluoroborate, ([BMIM]BF_4, $C_8H_{15}BF_4N_2$, Fluka, >97%) and diethylene glycol (DEG) (Sigma-Aldrich, 99%) were used as the fluoride source and as the solvent respectively. For the preparation of paste, ethyl cellulose (Sigma-Aldrich, powder) was used as the organic binder and α-terpineol (SAFC, ≥96%) was used as a solvent. Commercial gold nanoparticles were purchased from Nanoimunotech.

Synthesis of up-converting nanoparticles

Yttrium fluoride nanoparticles doped with 20% ytterbium and 2% of erbium were synthesized following a procedure previously reported.[22,25] In brief, YCl_3 (1.872 mmol) and $YbCl_3$ (0.48 mmmol) were dissolved together in DEG (105.6 ml) under magnetic stirring and heating at 70 °C, and $ErCl_3$ (0.048 mmol) was dissolved in another vial containing 12 mL of DEG at the same conditions. After dissolving, $ErCl_3$ was added to a solution of YCl_3 and $YbCl_3$ precursors, then the mixture was cooled to room temperature. Consequently, 2.4 mL of [BMIM]BF_4 was poured onto this above mixture keeping the magnetic stirring for few minutes at room temperature to obtain a homogeneous mixture. The final solution was heated at 120 °C for 15 hours, then cooled to room temperature. The resulting particles were centrifuged and cleaned three times with absolute ethanol, then dispersed in ethanol for the paste preparation.

Nanophosphor paste preparation

Reference paste was carried out following a procedure previously reported.[22] Briefly, nanophosphor particles, with mass m_{np}, were dispersed in ethanol and sonicated with a tip sonicator for 10 min to minimize the aggregation of particles. An amount of 0.3 m_{np} of ethyl cellulose was added to the nanophosphor particle suspension, followed by a process of magnetic stirring for 5 min and tip sonication for another 5 min. Subsequently, an amount of 4 m_{np} of α-terpineol was added, following the same sequence of magnetic stirring and tip sonication. Finally, the evaporation of solvent at reduced pressure resulted in a viscous paste. Pastes containing gold NPs were fabricated following the same procedure but with the addition of the desired amounts of gold NPs in the suspension of nanophosphor particles (see Fig. 1a).

Nanophosphor film preparation

Nanophosphor films without and with embedded gold nanoparticles were prepared using a blade coating method. A fraction of nanophosphor paste, without or with gold nanoparticles incorporated, was placed on a glass substrate and extended over it (see Fig. 1b).[22] The resulting films were annealed for 30 minutes in a hot plate at 400 °C with a rate of 2 °C per minute.

Morphological and structural characterization

Transmission electron microscopy (TEM) (Philips, Model 200CM) was selected to disclose the shape and size of the synthesized nanophosphor particles. Top view and cross section of annealed nanophosphor particle films without and with embedded gold nanoparticles were obtained using Scanning Electron Microscopy (SEM) (Hitachi Model S4800 microscope). The structural properties of those films were characterized using X-ray diffraction (XRD). XRD patterns were obtained using a Panalytical X'pert Pro.

Optical characterization

Total transmittance (T_{tot}) and total reflectance (R_{tot}) were measured using an UV-vis-IR spectrophotometer Cary 7000 equipped with an integrating sphere. The absorptance was calculated using the following equation.

$$A = 1 - T_{tot} - R_{tot}.$$

Photoluminescence (PL) and PL decay measurements were performed using a spectrofluorometer (Edinburgh Instruments, Model FLS1000). As an excitation source, we used a 980 nm laser (2 W of optical power) operating at maximum power in continuous mode for static UC measurements and in pulsed mode (repetition rate of 250 Hz and pulse width of 360 μs) for time-dependent PL intensity analysis. A computer control neutral density filter wheel was applied before the sample to study the power dependence of UCPL intensity.

Lifetime analysis

Time-dependent UCPL results were analyzed using FAST software from Edinburgh, taking into account the instrumental response function using the Exponential Component Analysis (Reconvolution) model.

Conflicts of interest

The authors declare no competing financial interest.

Acknowledgements

This project is financially supported by the European Research Council (ERC) under the European Union's Horizon 2020 Research and Innovation Programme (NANOPHOM, grant agreement no. 715832). T. T. N. is thankful to MCIN/AEI/10.13039/501100011033 and European Union Next GenerationEU/PRTR for funding her Juan de la Cierva Formación contract.

References

1 A. Das, K. Bae and W. Park, *Nanophotonics*, 2020, **9**, 1359–1371.
2 C. Duan, L. Liang, L. Li, R. Zhang and Z. P. Xu, *J. Mater. Chem. B*, 2018, **6**, 192–209.
3 G. Kakavelakis, K. Petridis and E. Kymakis, *J. Mater. Chem. A*, 2017, **5**, 21604–21624.
4 X. Peng, B. Huang, R. Pu, H. Liu, T. Zhang, J. Widengren, Q. Zhan and H. Ågren, *Nanoscale*, 2019, **11**, 1563–1569.
5 E. D. Martínez, C. D. S. Brites, L. D. Carlos, A. F. García-Flores, R. R. Urbano and C. Rettori, *Adv. Funct. Mater.*, 2019, **29**, 1807758.
6 N. Kiseleva, D. Busko, B. S. Richards, M. A. Filatov and A. Turshatov, *J. Phys. Chem. Lett.*, 2020, **11**, 6560–6566.
7 J.-C. Boyer and F. C. J. M. van Veggel, *Nanoscale*, 2010, **2**, 1417.
8 S. Fan, G. Gao, S. Sun, S. Fan, H. Sun and L. Hu, *J. Mater. Chem. C*, 2018, **6**, 5453–5461.
9 D. Hudry, D. Busko, R. Popescu, D. Gerthsen, I. A. Howard and B. S. Richards, *J. Mater. Chem. C*, 2019, **7**, 7371–7377.
10 S. Wen, J. Zhou, K. Zheng, A. Bednarkiewicz, X. Liu and D. Jin, *Nat. Commun.*, 2018, **9**, 2415.
11 R. Rafique, S. H. Baek, L. M. T. Phan, S.-J. Chang, A. R. Gul and T. J. Park, *Mater. Sci. Eng. Carbon*, 2019, **99**, 1067–1074.
12 S. Enoch and N. Bonod, ed., *Plasmonics: From Basics to Advanced Topics*, Springer Berlin Heidelberg, Berlin, Heidelberg, 2012, vol. 167.
13 X. Qin, A. N. Carneiro Neto, R. L. Longo, Y. Wu, O. L. Malta and X. Liu, *J. Phys. Chem. Lett.*, 2021, **12**, 1520–1541.
14 J. Dong, W. Gao, Q. Han, Y. Wang, J. Qi, X. Yan and M. Sun, *Rev. Phys.*, 2019, **4**, 100026.
15 W. Xu, X. Chen and H. Song, *Nano Today*, 2017, **17**, 54–78.
16 D. M. Wu, A. García-Etxarri, A. Salleo and J. A. Dionne, *J. Phys. Chem. Lett.*, 2014, **5**, 4020–4031.
17 M. Fujii, T. Nakano, K. Imakita and S. Hayashi, *J. Phys. Chem. C*, 2013, **117**, 1113–1120.
18 J. He, W. Zheng, F. Ligmajer, C.-F. Chan, Z. Bao, K.-L. Wong, X. Chen, J. Hao, J. Dai, S.-F. Yu and D. Y. Lei, *Light: Sci. Appl.*, 2017, **6**, e16217–e16217.
19 Y. Yang, Y. Cong, X. Lin, B. Cao, D. Dong, K. Liu, Y. Xiao, J. Shang, Y. Bao, Y. Liu, G. Fang, Y. Wang, Y. Chen, J. Zhang and B. Dong, *J. Mater. Chem. A*, 2020, **8**, 4040–4048.
20 Z. Yin, H. Li, W. Xu, S. Cui, D. Zhou, X. Chen, Y. Zhu, G. Qin and H. Song, *Adv. Mater.*, 2016, **28**, 2518–2525.
21 I. Ahn, S. J. Yeo, K. Jung, G. Kang, D. Shin, H. S. Jang, B. Kim, M. Nam, S. J. Kwon and D. Ko, *Adv. Funct. Mater.*, 2020, **30**, 1909445.
22 T. T. Ngo, E. Cabello-Olmo, E. Arroyo, A. I. Becerro, M. Ocaña, G. Lozano and H. Míguez, *ACS Appl. Mater. Interfaces*, 2021, **13**, 30051–30060.
23 J. M. Miranda-Muñoz, D. Geng, M. E. Calvo, G. Lozano and H. Míguez, *J. Mater. Chem. C*, 2019, **7**, 267–274.
24 E. Cabello-Olmo, P. Molet, A. Mihi, G. Lozano and H. Míguez, *Adv. Opt. Mater.*, 2021, **9**, 2001611.
25 N. O. Nuñez, M. Quintanilla, E. Cantelar, F. Cussó and M. Ocaña, *J. Nanopart. Res.*, 2010, **12**, 2553–2565.
26 G. Chai, G. Dong, J. Qiu, Q. Zhang and Z. Yang, *Sci. Rep.*, 2013, **3**, 1598.
27 L. Sun, J. Pan, X. Zhang, H. Wang, L. Li and Y. Yu, *RSC Adv.*, 2015, **5**, 77673–77681.
28 D. Mendez-Gonzalez, S. Melle, O. G. Calderón, M. Laurenti, E. Cabrera-Granado, A. Egatz-Gómez, E. López-Cabarcos, J. Rubio-Retama and E. Díaz, *Nanoscale*, 2019, **11**, 13832–13844.
29 M. Saboktakin, X. Ye, S. J. Oh, S.-H. Hong, A. T. Fafarman, U. K. Chettiar, N. Engheta, C. B. Murray and C. R. Kagan, *ACS Nano*, 2012, **6**, 8758–8766.
30 K. K. Haldar and A. Patra, *Appl. Phys. Lett.*, 2009, **95**, 063103.
31 T. Ung, L. M. Liz-Marzán and P. Mulvaney, *J. Phys. Chem. B*, 2001, **105**, 3441–3452.
32 R. Arppe, I. Hyppänen, N. Perälä, R. Peltomaa, M. Kaiser, C. Würth, S. Christ, U. Resch-Genger, M. Schäferling and T. Soukka, *Nanoscale*, 2015, **7**, 11746–11757.

33 D. Przybylska and T. Grzyb, *J. Mater. Sci.*, 2020, **55**, 14166–14178.
34 C. Liu and D. Chen, *J. Mater. Chem.*, 2007, **17**, 3875.
35 T. Hinamoto, T. Higashiura, H. Sugimoto and M. Fujii, *J. Phys. Chem. C*, 2019, **123**, 25809–25815.
36 J. Zhou, Q. Liu, W. Feng, Y. Sun and F. Li, *Chem. Rev.*, 2015, **115**, 395–465.
37 F. Wang and X. Liu, *Chem. Soc. Rev.*, 2009, **38**, 976.
38 Y. Shang, J. Zhou, Y. Cai, F. Wang, A. Fernandez-Bravo, C. Yang, L. Jiang and D. Jin, *Nat. Commun.*, 2020, **11**, 6156.
39 Q.-C. Sun, H. Mundoor, J. C. Ribot, V. Singh, I. I. Smalyukh and P. Nagpal, *Nano Lett.*, 2014, **14**, 101–106.
40 D. Lu, C. Mao, S. K. Cho, S. Ahn and W. Park, *Sci. Rep.*, 2016, **6**, 18894.
41 J. Liu, Q. Wang, X. Sang, H. Hu, S. Li, D. Zhang, C. Liu, Q. Wang, B. Zhang, W. Wang and F. Song, *Nanomaterials*, 2021, **11**, 1037.
42 W. Ge, X. R. Zhang, M. Liu, Z. W. Lei, R. J. Knize and Y. Lu, *Theranostics*, 2013, **3**, 282–288.
43 P. Yuan, Y. H. Lee, M. K. Gnanasammandhan, Z. Guan, Y. Zhang and Q.-H. Xu, *Nanoscale*, 2012, **4**, 5132.
44 F. Kang, J. He, T. Sun, Z. Y. Bao, F. Wang and D. Y. Lei, *Adv. Funct. Mater.*, 2017, **27**, 1701842.
45 W. Park, D. Lu and S. Ahn, *Chem. Soc. Rev.*, 2015, **44**, 2940–2962.
46 S. K. Maurya, S. P. Tiwari, A. Kumar and K. Kumar, *J. Rare Earths*, 2018, **36**, 903–910.
47 L. Tao, W. Xu, Y. Zhu, L. Xu, H. Zhu, Y. Liu, S. Xu, P. Zhou and H. Song, *J. Mater. Chem. C*, 2014, **2**, 4186–4195.
48 G. Y. Lee, K. Jung, H. S. Jang, J. Kyhm, I. K. Han, B. Park, H. Ju, S. J. Kwon and H. Ko, *Nanoscale*, 2016, **8**, 2071–2080.
49 D. Lu, S. K. Cho, S. Ahn, L. Brun, C. J. Summers and W. Park, *ACS Nano*, 2014, **8**, 7780–7792.
50 A. Chu, H. He, Z. Yin, R. Peng, H. Yang, X. Gao, D. Luo, R. Chen, G. Xing and Y. J. Liu, *ACS Appl. Mater. Interfaces*, 2020, **12**, 1292–1298.
51 L. Novotny and B. Hecht, *Principles of Nano-Optics*, Cambridge University Press, Cambridge, 2nd edn, 2012.
52 R. E. Joseph and C. Jime, *J. Phys. Chem. A*, 2019, **123**(31), 6799–6811.
53 J. F. Suyver, A. Aebischer, S. García-Revilla, P. Gerner and H. U. Güdel, *Phys. Rev. B: Condens. Matter Mater. Phys.*, 2005, **71**, 125123.
54 J. Christiansen, H. Lakhotiya, E. Eriksen, S. P. Madsen, P. Balling and B. Julsgaard, *J. Appl. Phys.*, 2019, **125**, 043106.
55 C. Mao, K. Min, K. Bae, S. Cho, T. Xu, H. Jeon and W. Park, *ACS Photonics*, 2019, 7.
56 Y. Wu, X. Shen, S. Dai, Y. Xu, F. Chen, C. Lin, T. Xu and Q. Nie, *J. Phys. Chem. C*, 2011, **115**, 25040–25045.
57 H. Liu, C. T. Xu, D. Lindgren, H. Xie, D. Thomas, C. Gundlach and S. Andersson-Engels, *Nanoscale*, 2013, **5**, 4770–4775.
58 C. Mao, K. Min, K. Bae, S. Cho, T. Xu, H. Jeon and W. Park, *ACS Photonics*, 2019, **6**, 1882–1888.
59 A. Das, C. Mao, S. Cho, K. Kim and W. Park, *Nat. Commun.*, 2018, **9**, 4828.